International Journal of Rock Mechanics & Mining Sciences 204 (2026) 106583

Contents lists available at ScienceDirect

International Journal of Rock Mechanics and Mining Sciences

journal homepage: www.elsevier.com/locate/ijrmms

Evaluation of CO_2 sequestration potential in shale reservoirs using an improved embedded discrete fracture model

Zhiming Chen [a], Biao Zhou [a,*], Olufemi Olorode [b], Wei Yu [c], Kamy Sepehrnoori [c]

[a] Hainan Institute of China University of Petroleum (Beijing), China University of Petroleum (Beijing), Beijing, China
[b] Craft and Hawkins Department of Petroleum Engineering, Louisiana State University, Baton Rouge, LA, USA
[c] Hildebrand Department of Petroleum and Geosystems Engineering, The University of Texas at Austin, Austin, TX, USA

ARTICLE INFO

Keywords:
CO_2 sequestration
Shale
Embedded discrete fracture model
Transient flow

ABSTRACT

CO_2 capture, utilization, and storage in depleted petroleum reservoirs is one of the rapidly growing areas of research in the petroleum industry. Of these reservoirs, shale gas reservoirs are particularly promising, considering the potential for trapping the injected CO_2 by sorption, in addition to other trapping mechanisms expected in other subsurface reservoirs. However, accurate characterization of the pressure transient behaviors during CO_2 injection is imperative for the estimation of reservoir properties and CO_2 storage capacity. The accuracy of standard models for capturing transient flow dynamics remains limited in representing the early-time interactions between fractures and the surrounding matrix. To address these limitations, this study proposes an Analytically Projected Embedded Discrete Fracture Model (AEDFM), in which fractures are projected onto all six faces of three-dimensional host matrix elements. This approach systematically incorporates the influence of surrounding matrix blocks, enabling a more accurate simulation of the CO_2 pressure transient behaviors of multi-stage fractured horizontal wells (MFHWs) in shale gas reservoirs. The accuracy of the proposed model is validated against reference solutions.

Utilizing the proposed AEDFM, we developed a workflow for CO_2 storage capacity evaluation based on pressure transient analysis. Furthermore, we analyzed the impact of fracture and reservoir parameters on pressure response and CO_2 storage performance. Based on pressure test data from a shale gas well in the Longmaxi formation, reservoir rock properties, such as permeability, were obtained through curve matching. Using the matched property values, the CO_2 storage capacity was evaluated at different injection rates. Overall, the proposed model offers an efficient and accurate framework for analyzing transient flow and assessing CO_2 storage capacity in shale reservoirs.

1. Introduction

The combination of horizontal drilling and hydraulic fracturing has facilitated the efficient development of shale gas resources.[1] With the proliferation of shale gas wells over the past 20 years, several researchers have investigated the concept of carbon dioxide (CO_2) injection into shale gas reservoirs to enhance natural gas recovery and simultaneously sequester some of the injected CO_2.[2,3] Furthermore, depleted shale gas reservoirs are generally regarded as optimal candidates for long-term CO_2 storage [4–7]. Conventionally, pressure transient analysis has been a pivotal technique for characterizing reservoir properties, and it is now also being applied to evaluate the CO_2 storage potential.[8]

Analytical models offer certain advantages, including convenience and computational efficiency. Consequently, researchers have proposed analytical or semi-analytical models to investigate the pressure transient behaviors of CO_2 flow in petroleum reservoirs.[9] For instance, Su et al.[10] developed an analytical model to analyze the pressure transient behaviors of CO_2 flow, but the effects of adsorption and diffusion were neglected. Later, Chen et al.[11] proposed an analytical approach for pressure transient analysis during CO_2 injection and applied it to assess the CO_2 storage capacity in depleted shale gas reservoirs. However, the model assumed that the reservoir contained only CO_2 and that CO_2 properties, such as viscosity, remained constant. Furthermore, Xiao et al.[12] developed a semi-analytical model to analyze the pressure and rate transient behaviors during CO_2 injection. This model incorporates

* Corresponding author.
E-mail address: zhoubiao1228@163.com (B. Zhou).

https://doi.org/10.1016/j.ijrmms.2026.106583
Received 18 March 2026; Received in revised form 29 April 2026; Accepted 20 May 2026
1365-1609/© 2026 Elsevier Ltd. All rights are reserved, including those for text and data mining, AI training, and similar technologies.

effects such as desorption, adsorption, and stress sensitivity. It assumes that the hydraulic fractures are fully penetrating the formation and that the natural fractures in the reservoir can be represented using the dual-porosity model. However, due to the complex flow mechanisms and the presence of natural fractures across multiple scales in shale formations, these conventional analytical and semi-analytical models are unable to accurately capture the transient pressure and rate behaviors of CO_2 injection in shale reservoirs.

Given the widespread presence of natural and hydraulic fractures in shale reservoirs, the accurate and effective simulation of fluid flow has attracted considerable attention from researchers [13–17]. The discrete fracture model (DFM) was developed to accurately simulate fractured reservoirs, but it requires unstructured grids that conform to the geometry of the fractures within the reservoir.[18] This causes excessive meshing requirements in complex three-dimensional (3D) fractured reservoirs, thereby greatly increasing computational expense.[19]

The EDFM was developed to overcome the substantial computational cost associated with the DFM.[20] Its core concept is to represent fractures as lower-dimensional elements (typically 2D) embedded within a 3D matrix grid that does not need to conform explicitly to the fracture geometry.[21] By introducing non-neighboring connections (NNCs) between fracture cells and adjacent matrix cells, EDFM enables fluid exchange between fractures and the surrounding matrix without requiring conforming meshes. This significantly simplifies grid generation and improves computational efficiency.[22] Despite these advantages, later studies revealed several limitations of the EDFM approach. In particular, EDFM commonly relies on permeability approximations derived from geometric parameters when modelling low-permeability fractures, fracture tips, and fracture intersections.[23] Moreover, the method generally assumes a linear pressure distribution between fractures and the matrix, which can reduce the accuracy of local flow characterization, underestimate flow behavior, and introduce local numerical errors. To address these shortcomings, several enhanced EDFM formulations have been proposed.[24] For example, Losapio, Scotti[25] proposed the Local EDFM (LEDFM), in which locally refined grids are generated around fractures to more accurately calculate transmissibility between fractures and the surrounding porous medium, as well as within the nearby matrix region. By relaxing the linear pressure distribution assumption adopted in conventional EDFM, LEDFM improves the accuracy of flow simulations. In addition, Olorode, Rashid[26] developed the transient EDFM (tEDFM), which incorporates a transient correction factor into the non-neighboring connection (NNC) transmissibility calculations of conventional EDFM, thereby enhancing the accuracy of early-time flow simulations. Furthermore, Zhou et al.[27] accounted for the time-dependent evolution of the transient correction factor and proposed an analytically modified EDFM for pressure transient analysis. Guo et al.[28] proposed an enriched embedded discrete fracture model (nEDFM) that extends EDFM to arbitrary intersections of conductive and blocking fractures by reconstructing local shape functions and improving the star-delta formulation, thereby significantly enhancing the accuracy and applicability of non-conforming grid simulations for complex fractured reservoirs.

To overcome the EDFM's limitations associated with low-conductivity fractures, Tene et al.[20] initially proposed the pEDFM. In this method, the projection areas of fractures onto adjacent matrix cell surfaces are explicitly calculated, enabling more accurate simulation of low-conductivity fractures. Subsequently, Jiang, Younis[29] improved the pEDFM framework by introducing additional physical constraints during the preprocessing stage, thereby enhancing its physical consistency. In addition, Rao et al.[30] advanced the method by developing a pragmatic "Micro-Translation Method" to determine the optimal combination of projection faces in pEDFM. They also incorporated fracture–fracture connections, which further extended the applicability of the framework. Meanwhile, Olorode et al.[31] proposed a 3D pEDFM algorithm capable of modelling naturally fractured systems with arbitrarily oriented fractures in 3D domains. Furthermore, Rashid, Olorode[32] developed the Continuous Projection Embedded Discrete Fracture Model (CPEDFM), which ensures continuous projections of inclined fractures on cell surfaces in 3D simulations, thereby improving the physical representation of low-conductivity fracture systems.

In addition, many researchers have applied EDFM and pEDFM to simulate CO_2 flow.[33,34] For example, Zuloaga-Molero et al.[35] applied EDFM to simulate CO_2-enhanced oil recovery (EOR) in tight oil reservoirs. Zhao et al.[36] developed a CO_2 injection numerical model based on EDFM that incorporates multiple flow mechanisms. Furthermore, Jia et al.[37] applied pEDFM to simulate the CO_2 injection and recovery process in shale-oil reservoirs. However, these studies have primarily focused on pressure and rate behaviors over large time scales during CO_2 injection, with limited attention given to the pressure transient behaviors at early times.

Although extensive research has been conducted on EDFM and pEDFM, studies on the fast and accurate simulation of transient fluid flow in fractured reservoirs are limited. Efficient numerical models that can capture the pressure transient behaviors of CO_2 injection in shale reservoirs are also limited. However, accurately modeling such transient behavior is essential for analyzing injection conditions and estimating reservoir properties. To address these limitations, the traditional AEDFM framework is enhanced by integrating the projection concept from pEDFM. This involves projecting fractures onto all six faces of the primary matrix grid blocks. Connections are established between the fracture and each of the six adjacent matrix cells to fully account for the influence of the surrounding matrix on the fracture flow. This improvement significantly enhances the accuracy of the EDFM.

The accuracy of the proposed model is validated through comparison with the results from the analytical model. This study proposes an enhanced model for analyzing pressure transient behaviors during CO_2 injection in shale reservoirs. Furthermore, it develops a workflow for evaluating CO_2 storage capacity using pressure transient analysis. Moreover, parametric studies are conducted to evaluate the influence of fracture properties and reservoir parameters on the pressure response and CO_2 storage capacity. Finally, based on pressure test data from a shale gas well in the Longmaxi Formation, reservoir properties such as permeability were obtained through curve matching. Using the matched reservoir properties, the CO_2 storage capacity was evaluated at different injection rates. This study provides an efficient and accurate tool for analyzing complex transient fluid flow in fractured reservoirs and for evaluating CO_2 storage potential.

2. Theory

2.1. Physical model

Fig. 1 illustrates the physical model of an MFHW in a depleted shale gas reservoir with natural fractures. To establish the mathematical model, the following assumptions are made:

(1) Hydraulic fractures are rectangular in shape, and natural fractures are polygonal.
(2) The effects of temperature and gravity are neglected.
(3) Fluid flow obeys Darcy's law.
(4) Fluid is injected at a constant rate and enters the formation only through hydraulic fractures.
(5) A homogeneous reservoir with closed boundaries is assumed to facilitate parametric sensitivity analysis.

2.2. Mathematical model

It is assumed that the fluid in the shale gas reservoir exists exclusively in the vapor phase and consists of CO_2, CH_4, C_2H_6, and C_3H_8, etc. Conversely, the injected fluid is assumed to be pure CO_2. Adsorption is one of the most important mechanisms for geological storage of CO_2[38]. The Langmuir isotherm is used to account for gas adsorption/desorption

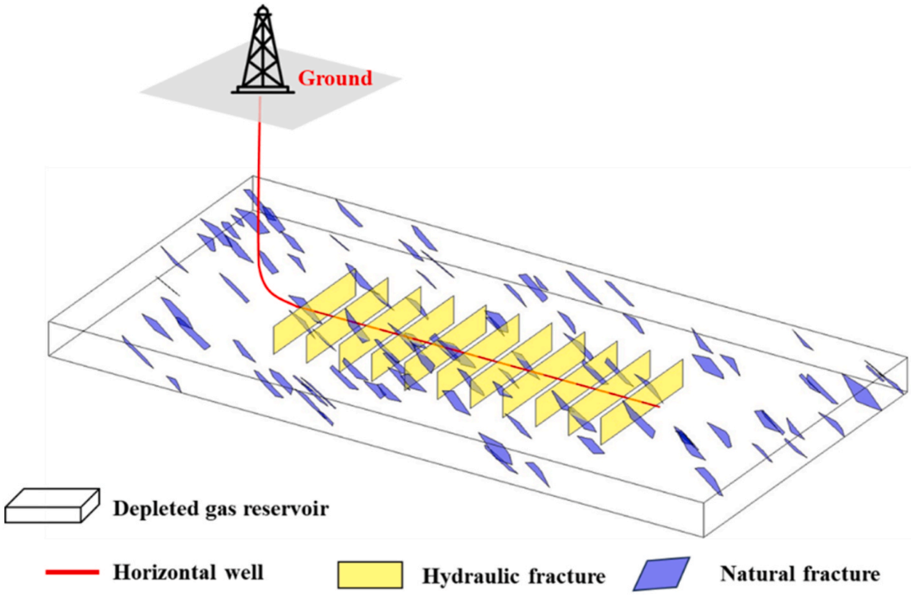

Fig. 1. The physical model.

effects, and Fick's law is applied to model gas diffusion.[39] Therefore, the mass conservation equation for a multicomponent gas in EDFM can be expressed as follows:

$$\frac{\partial}{\partial t}\left[\phi \sum \rho_v X_v^i + \delta_s(1-\phi)\rho_s^i\right] + \sum \nabla \cdot \left(\rho_v X_v^i \overrightarrow{v_v} + J_v^i\right) - \sum \rho_v X_v^i q_v \Big/ V + q_i^{nnc} \Big/ V = 0 \tag{1}$$

$$\overrightarrow{v_v} = -\frac{k}{\mu}\nabla p \tag{2}$$

$$\rho_s^i = \rho_{sL}^i \frac{y_i \frac{p}{p_L^i}}{1 + \sum_{j=1}^n y_j \frac{p}{p_L^j}} \tag{3}$$

$$J_v^i = -D_v^i \nabla\left(\rho_v X_v^i\right) \tag{4}$$

where the subscript v denotes the vapor phase; the superscript i represents the i-th component in the vapor phase; ϕ, ρ, q, V, t, k and μ denote porosity, density, volumetric injection rate, grid-block volume, time, permeability and viscosity, respectively; δ_s is a logical parameter that is set to 1 only in the matrix; ρ_s and ρ_{sL} represent the sorbed-gas density of rock and the maximum sorbed-gas density of rock, respectively; $\overrightarrow{v_v}$ represents the Darcy velocity of the vapor phase; X_v^i and y_i represent the mass fraction and mole fraction of component i in the vapor phase, respectively; p and p_L represent the reservoir and Langmuir pressures, respectively; D_v^i represents the diffusion coefficient of component i in the vapor phase.

In Eq. (1), q_i^{nnc} denotes the mass flow rate of component i exchanged through non-neighboring connections (NNCs), and is defined as[40]:

$$q_i^{nnc} = T_f \sum_{n=1}^{N} A_n^{nnc} \frac{k_n^{nnc}}{\mu} \rho_v X_v^i \left(\frac{p - p_n^{nnc}}{d_n^{nnc}}\right) \tag{5}$$

$$T_f = \frac{1}{2} + \frac{1}{2}\left[1 - \exp\left(-3\pi^2 k_m t / \phi_m \mu C_t a_m^2\right)\right]^{-\frac{1}{2}} \tag{6}$$

where A^{nnc} , k^{nnc} and d^{nnc} denote area, permeability and distance of NNCs, respectively; T_f denotes the transient factor; the superscript m represents the matrix; C_t denotes the total compressibility; a_m^2 represents the area where the fracture intersects with the matrix grid.

Although the reservoir is three-dimensional, the AEDFM simplifies the local matrix-fracture interaction into a flow problem normal to the fracture planes. This is based on the physical reality that the high permeability contrast forces fluid to move predominantly in the direction of the steepest pressure gradient, which is orthogonal to the fracture surface. By applying this dimension-reduction strategy, the 1D analytical transient factor T_f effectively captures the transient flow while maintaining high computational efficiency.

The transmissibility coefficient for an NNC is derived to characterizefluid exchange between fracture segments and their host matrix cells. The transmissibility coefficient can be written as follows[31]:

$$T^{nnc} = \frac{k^{nnc} A^{nnc}}{d^{nnc}} \tag{7}$$

While conventional EDFM accounts for fluid exchange between-fractures and the matrix cells containing them, it only accounts for flow interactions between the fracture-hosting cell and its directly adjacent matrix cells. This approach has been demonstrated to weaken the influence of the surrounding matrix domain on fracture dynamics, especially at refined grid resolution.[27] To more accurately capture the early-time transient flow behavior near fractures, an enhanced projection method based on the pEDFM framework is proposed. This is referred to as AEDFM. Specifically, the fracture is geometrically projected onto all six faces of the surrounding matrix grid cells, thereby systematically capturing the influence of the surrounding matrix domains on fracture flow behavior. The schematic of the AEDFM projection is illustrated in Fig. 2(a), in which the fracture projections onto four matrix faces in the YZ and XY planes are demonstrated. To ensure numerical stability and pressure continuity, the projection weight for each fracture segment is calculated independently within its corresponding matrix grid cell.

The traditional pEDFM projects the fracture only onto three faces of the matrix grid on one side of the fracture, for example, the right, bottom, and front faces. Compared to EDFM, pEDFM introduces additional NNCs between the projected matrix grid cells and the fracture cells. These can be expressed as follows:

$$T_{pM-F}^{nnc} = \frac{A_{if\perp\overrightarrow{x}} k_{pM-F}^{nnc}}{d_{pM-F}^{nnc}} \tag{8}$$

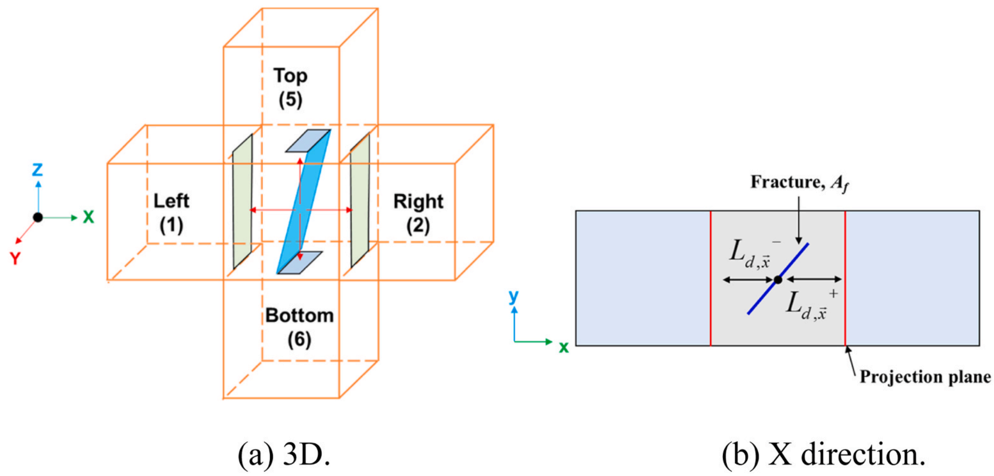

Fig. 2. The schematic diagram of the projection of AEDFM.

$$k^{nnc}_{pM-F} = \frac{k_{pM} k_f}{k_{pM} + k_f} \tag{9}$$

where $A_{if\perp\vec{x}}$ denotes the area in each projection direction; $\vec{x}$ represents the X, Y and Z directions; the subscript pM denotes the projected matrix cell; he subscript $pM - F$ denotes the connection between the projected matrix cell and the fracture cell.

Due to the addition of connections between the projected matrix cells and the fracture, the original connections between the projected matrix cells and the matrix cell are weakened:

$$T^{nnc}_{pM-M} = T_{M-M} \frac{A_{ii} - A_{if\perp\vec{x}}}{A_{ii}} \tag{10}$$

The development of pEDFM was originally motivated by the requirement to simulate low-conductivity fractures. In the context of high-conductivity fractures, the application of this method may lead to pressure asymmetry on both sides of the fracture. To more accurately simulate transient flow near and within fractures, AEDFM is built upon the idea of pEDFM by projecting the fracture onto all six faces of the surrounding matrix grid cells. The transmissibility between the projected matrix cells and the fracture is given by:

$$T^{nnc}_{pM-F} = \frac{\beta_{\vec{x}_i} A_{if\perp\vec{x}} k^{nnc}_{FPM-F}}{d^{nnc}_{FPM-F}} \tag{11}$$

where $\beta_{\vec{x}}$ is the projection weight corresponding to the projected matrix grid. It is defined as follows:

$$\beta_{\vec{x}} = \begin{cases} \dfrac{L_{d,\vec{x}}^{-}}{L_{d,\vec{x}}^{-} + L_{d,\vec{x}}^{+}}, \textit{positive direction} \\ \dfrac{L_{d,\vec{x}}^{+}}{L_{d,\vec{x}}^{-} + L_{d,\vec{x}}^{+}}, \textit{negative direction} \end{cases} \tag{12}$$

$$L_d = \frac{1}{A_f} \int_{S_f} |(\mathbf{x} - \mathbf{x}_d) \cdot \mathbf{n}_d| dA \tag{13}$$

where L_d denotes the average distance from the fracture -plane to the projection plane, as illustrated in Fig. 2(b); The superscripts + and - denote the positive and negative directions respectively; A_f is the area of the fracture; $\mathbf{x}$ is any point on the fracture plane; $\mathbf{x}_d$ is any point on the projection plane; $\mathbf{n}_d$ is the normal vector of the projection plane. Fig. 2 (b) illustrates the calculation of projection weights in the x-direction for the two-dimensional case. First, the average distance from the fracture surface to the projection plane in each direction is computed. Then, the projection weights are determined based on the ratio of these average distances. As shown in Eq. (12), the closer the fracture plane is to a projected matrix plane, the stronger the influence of the corresponding projected matrix cell on the fracture. Therefore, the projection weight on that side should be larger. Accordingly, the projection weight is defined as the ratio of the average distance from the fracture to the projected matrix plane on the opposite side to the sum of the average distances from the fracture to the projected planes on both sides.

To maintain mass conservation when introducing connections between projected matrix cells and fractures, the original transmissibility between projected matrix cells and their host matrix cells must be systematically attenuated. This adjustment prevents the overcounting of flux pathways while preserving the physical integrity of flow interactions. The modified transmissibility is formulated as follows:

$$T^{nnc}_{pM-M} = T_{M-M} \frac{A_{ii} - \beta_{\vec{x}} A_{if\perp\vec{x}}}{A_{ii}} \tag{14}$$

By incorporating the transient factor derived from the analytical solution, the developed model is referred to as the analytically projected EDFM (AEDFM).

During the processes of fluid extraction or injection, changes in reservoir pore pressure can lead to variations in permeability due to stress sensitivity. The exponential evaluation model is adopted to characterize this permeability variation[41]:

$$k = K_0 \exp[-\alpha_k (p_0 - p)] \tag{15}$$

where K_0 denotes the permeability without confining pressure; α_k denotes the stress sensitivity coefficient.

Furthermore, considering the wellbore storage effect, the wellbore flow equation can be expressed as:

$$Q \Big/ B = \frac{2\pi k_f w_f}{\mu \ln(r_e / r_w)} \left(p_e - p_{wf}\right) + 24C \frac{\partial p_{wf}}{\partial t} \tag{16}$$

$$r_e = 0.14\sqrt{L^2 + W^2} \tag{17}$$

where Q, B, k_f, w_f, r_w and C denote the flow rate at the surface, the volume factor, the fracture permeability, the fracture width, the well radius, and the wellbore storage coefficient, respectively; p_e and p_{wf} denote the perforation pressure and bottomhole pressure, respectively; L and W denote the fracture length and fracture height, respectively.

2.3. Numerical solution

The governing equations and wellbore equation are discretized using the backward Euler scheme and the finite volume method.[42] The discretized forms of Eqs. (1) and (15) are given as follows:

$$\frac{1}{\Delta t}\left\{\left[\phi\sum\rho_v X_v^i+\delta_s(1-\phi)\rho_s^i\right]^{n+1}-\left[\phi\sum\rho_v X_v^i+\delta_s(1-\phi)\rho_s^i\right]^{n}\right\}+\sum div\left(\rho_v X_v^i\overrightarrow{v_v}+J_v^i\right)^{n+1}-\sum\left(\rho_v X_v^i q_v\right)^{n+1}\Big/V+\left(q_i^{nnc}\right)^{n+1}\Big/V=R_i^{n+1} \tag{18}$$

$$(Q/B)^{n+1}=\frac{2\pi k_f w_f}{\mu^{n+1}\ln(r_e/r_w)}\left(p_e-p_{wf}\right)^{n+1}+24C\frac{p_{wf}^{n+1}-p_{wf}^{n}}{\Delta t} \tag{19}$$

where R denotes the residual value.

The above modifications are implemented based on the open-source framework MRST,[43] and transient pressure and rate solutions are obtained using automatic differentiation and Newton-Raphson iteration.

3. Results and discussions

3.1. Verification

To validate the accuracy of the improved AEDFM in simulating transient CO_2 flow, a model containing 11 hydraulic fractures was constructed using both the AEDFM and the analytical model. The AEDFM employed a structured Cartesian grid without local grid refinement, with a grid size of 20 × 20 × 20 m and a total of only 10,088 cells. The basic input parameters of the model are listed in Table 1. Considering that CO_2 is mainly injected into depleted gas reservoirs, the initial pressure was set to 5 MPa[44] and assumed to be uniformly distributed throughout the reservoir. In addition, due to inherent limitations of the analytical model, the effects of diffusion and natural fractures were not considered in this section. The results obtained from the AEDFM were then compared with those from the analytical model,[11] as shown in Fig. 3(a). Furthermore, the results of standard EDFM and tEDFM were generated using the same Cartesian grid as the AEDFM. Fig. 3(b) presents a comparative analysis of the simulation results from AEDFM, EDFM, and tEDFM.

As shown in Fig. 3(a), the log–log plots of pressure change and its derivative demonstrate that the AEDFM results match the analytical solution closely. The L^2 relative errors for pressure change and its derivative are 0.0186 and 0.0492, respectively. These low error magnitudes confirm the high accuracy and robustness of the proposed AEDFM in simulating transient CO_2 flow.

As shown in Fig. 3(b), the standard EDFM in MRST shows notable discrepancies from the reference solution during the early and middle flow periods, as evidenced by pronounced deviations in curve shape. These observations further highlight the superiority of the proposed AEDFM. Moreover, tEDFM tends to underestimate the pressure response in the early to middle stages, and its pressure derivative curve exhibits a more pronounced “dip.”

Furthermore, for a simulation spanning 70-time steps, the average total computation times over five runs were 58.6 s for EDFM, 59.1 s for tEDFM, and 59.5 s for AEDFM. Compared to EDFM, the computational cost of AEDFM increased by only 1.54%, while it remains highly competitive with tEDFM. The marginal time increase in AEDFM (approximately 0.7% over tEDFM) is primarily attributed to the analytical projection weight calculations. To ensure numerical stability and minimize discretization errors, a grid sensitivity analysis was conducted. The pressure derivative responses were compared across grid sizes of 40 m, 20 m, and 10 m. Taking the 10 m grid as the reference, the average relative errors for the 40 m and 20 m grids are 2.48% and 1.01% respectively. These results indicate that the AEDFM is robust to grid resolution and can provide high-precision solutions even with relatively coarse grids.

Table 1
Model parameters used for model verification.

Input Data	Value	Unit
Physical dimensions	2000 × 2000 × 20	m
Initial pressure	5	MPa
Matrix porosity	0.1	/
Matrix permeability	0.1	mD
Fracture permeability	10	D
Fracture aperture	0.01	m
Fracture half-length	80	m
Fracture height	16	m
Well radius	0.1	m
Skin factor	0.001	/
Wellbore storage coefficient	0.5	m^3/MPa
Injection rate	50000	m^3/d
Number of natural fractures	500	/
Natural fracture permeability	1	D

3.2. Flow regime identification

To more accurately analyze the pressure transient behaviors during CO_2 injection, the following flow regimes are identified based on the pressure derivative curve:

(1) Wellbore storage and skin effect. Due to wellbore storage and skin effects, the pressure derivative curve exhibits a unit-slope straight line and a characteristic "hump." This regime has been demonstrated to be a reliable method for estimating the wellbore storage coefficient and skin factor.
(2) Bilinear flow. A straight line with a slope of 1/4 appears on the pressure derivative curve, indicating fluid flow that is linear from the wellbore to the fracture and linear from the fracture into the reservoir.
(3) Linear flow. A slope of 1/2 on the pressure derivative curve indicates linear flow from the fracture into the reservoir. This stage can be used to estimate fracture parameters, such as fracture conductivity.
(4) Inter-fracture interference. Pressure waves from adjacent fractures interact, resulting in a rapid pressure increase and an upward trend in the pressure derivative, which reflects an increased apparent slope.
(5) Elliptical flow. A straight line with a slope of 1/3 appearing on the pressure derivative curve indicates that the fluid flow is approaching steady state, with pressure waves taking on an elliptical shape.
(6) Pseudo-radial flow. As the flow of fluid near the MFHW stabilizes, the pressure derivative curve flattens, forming a zero-slope straight line. This regime is generally employed to estimate reservoir permeability.

The division of flow regimes according to the characteristic features of the pressure derivative curves facilitates a more accurate analysis of flow behaviors and the inversion of reservoir parameters.[45]

4. Methodology

4.1. CO_2 storage potential evaluation

Fig. 4 presents a schematic workflow for evaluating CO_2 storage potential. For depleted shale reservoirs, key parameters such as reservoir permeability and fracture conductivity are first estimated using a numerical well test model based on geological information, hydraulic-fracturing data, and well-test data. These parameters are then used to update and refine the numerical well test model. Subsequently, the injection rate and the safety constrained pressure, which is typically lower than the original reservoir pressure, are determined by considering geological conditions, injection-facility requirements, and economic factors. Using the refined numerical model, the pressure transient behaviors during CO_2 injection are simulated. Based on the specified wellbore constrained injection pressure, the time required to reach this pressure is identified. The CO_2 storage capacity is then calculated as the

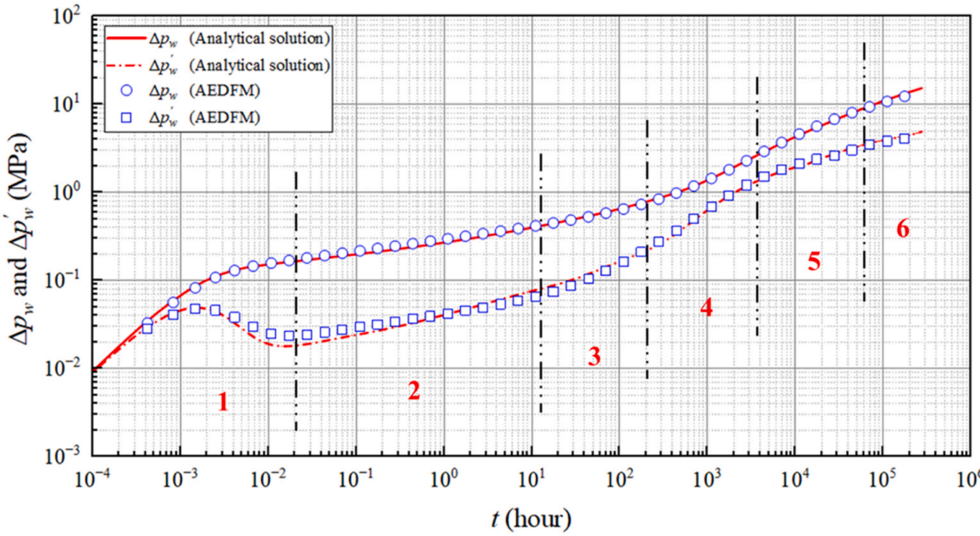

(a) Comparison of the analytical model and AEDFM.

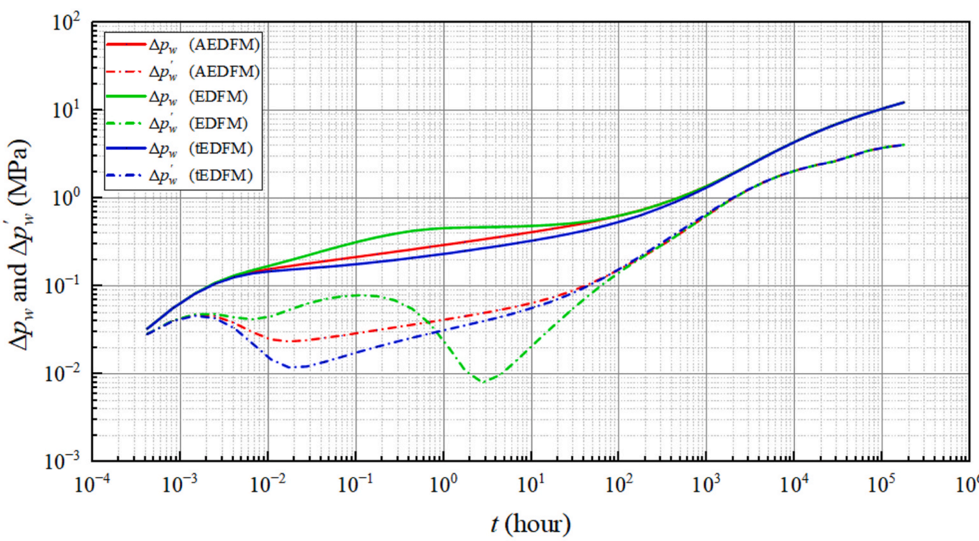

(b) Comparison of EDFM, tEDFM and AEDFM.

Fig. 3. Comparison of results from different models.

product of the injection rate and the injection duration.[11] It should be clarified that while Eq. (20) appears to be a product of injection rate and time, the adsorption effect is fully integrated into the pressure transient solution.

$$Q_T = Q \times t_{inj} \tag{20}$$

The constraint pressure was set to 10 MPa. It is anticipated that the bottomhole pressure of the injection well will reach the constraint pressure at approximately 580 days, as indicated by the pressure difference curve in Fig. 3. In this instance, the calculation of the CO_2 storage capacity is as follows:

$$Q_T = Q \times t_{inj} = 50000 \times 580 = 0.29 \times 10^8 \mathrm{m}^3 \tag{21}$$

4.2. Sensitivity analysis

To clarify the impact of injection parameters, fracture properties, and fluid-related parameters on the pressure transient behaviors during CO_2 injection, a series of sensitivity analyses are conducted. Considering long-term CO_2 sequestration, the pressure transient behaviors during 20 years of CO_2 injection are simulated.[46] The parameters under investigation include injection rate, fracture half-length, fracture conductivity, adsorption density, diffusion coefficient, and stress sensitivity coefficient. In this section, the influence of natural fractures is considered by randomly generating 1000 natural fractures using the Alghalandis discrete fracture network engineering (AEDFNE) method.[47] These natural fractures are primarily oriented in the NE–SW and NW–SE directions. The minimum fracture length is 40 m, the maximum is 60 m, and the average length is 50 m. The fracture aperture is 0.001 m, and the fracture conductivity is 1 mD·m. The spatial distribution of natural fractures is shown in Fig. 5.

4.2.1. Injection rate

As illustrated in Fig. 6, the pressure difference and pressure

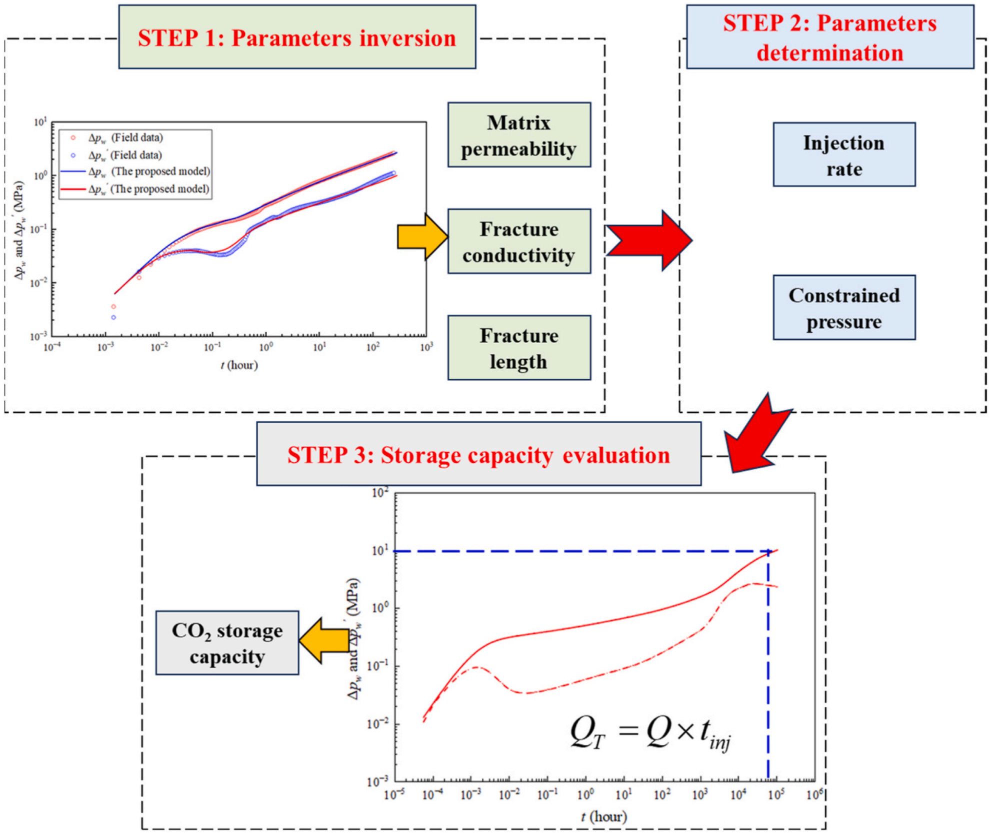

Fig. 4. Flow chart for CO_2 storage capacity evaluation.

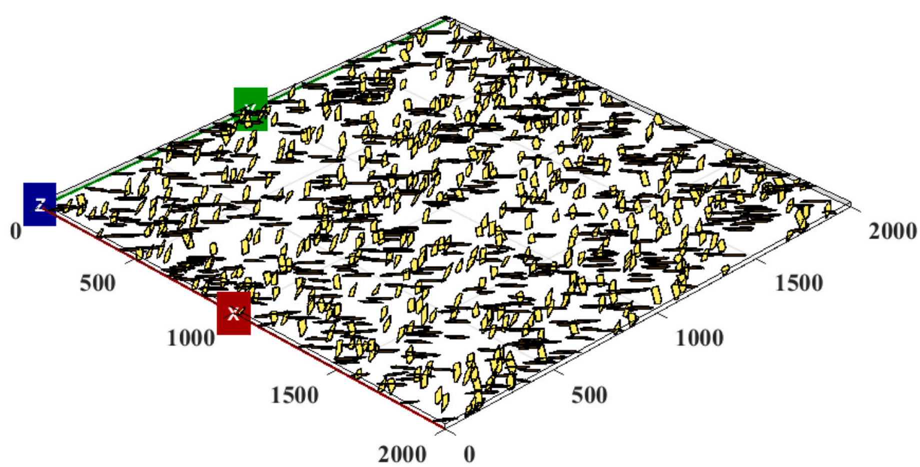

Fig. 5. The spatial distribution of natural fractures.

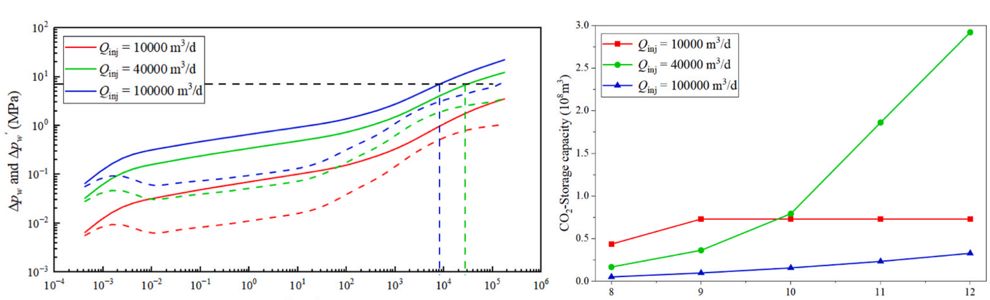

Fig. 6. Pressure curves and CO_2-storage capacity curves at different injection rates.

derivative curves are presented at various injection rates. It is evident that as the injection rate increases, there is a concomitant upward shift in both the pressure and pressure derivative curves, while their shapes remain comparable. This phenomenon can be attributed to the observation that elevated injection rates result in accelerated increases in bottomhole and reservoir pressure.

Additionally, Fig. 6 illustrates the CO_2 storage capacity at various constraint pressures and injection rates. When the injection rate is set at 10,000 m^3/d, the bottomhole pressure fails to reach the constraint pressure, even after a 20-year simulation period. This analysis yielded a CO_2 storage capacity of 0.730 × 10^8 m.^{3} It is noteworthy that the storage capacity at an injection rate of 40,000 m^3/d exceeds that at 100,000 m^3/d. When the constraint pressure is not higher than 9 MPa, the injection rate of 10,000 m^3/d yields the highest CO_2 storage capacity. In contrast, when the constraint pressure is set to 10 MPa, the injection durations for rates of 40,000 m^3/d and 100,000 m^3/d are approximately 1982 days and 157 days, respectively, corresponding to CO_2 storage capacities of 0.793 × 10^8 m^3 and 0.157 × 10^8 m.^{3} These results indicate that both excessively low and excessively high injection rates are unfavorable for optimizing CO_2 storage capacity. An excessively low injection rate will fail to fully utilize the CO_2 storage potential of the reservoir. Since the transmissibility between grid cells is fixed, a higher injection rate increases the flow between grid cells, necessitating a larger pressure drop, which in turn causes the bottomhole pressure to reach the constraint pressure rapidly. Thus, a reasonable injection rate should be selected in field practice to avoid overly aggressive injection rates.

4.2.2. *Fracture half-length*

Fig. 7 presents the pressure difference and pressure derivative curves for different fracture half-lengths. As the fracture length increases, the pressure response and its derivative shift later in time, indicating that interference between fractures occurs later. Additionally, the time required for the bottomhole pressure to reach the constraint pressure also increases with fracture length. The CO_2 storage capacity curves at different constraint pressures, as demonstrated in Fig. 7, indicate that higher constraint pressures and greater fracture lengths are more conducive to enhancing CO_2 storage capacity. At a constraint pressure of 12 MPa, the calculated CO_2 storage capacities for fracture half-lengths of 60 m, 80 m, and 120m are 0.514 × 10^8 m,^{3} 0.615 × 10^8 m,^{3} and 0.824 × 10^8 m,^{3} respectively. The storage capacity with a fracture half-length of 120 m is 60.3% higher than that with a fracture half-length of 60 m. These results indicate that, at a constant injection rate, longer fractures significantly enhance CO_2 storage capacity.

4.2.3. *Number of hydraulic fractures*

As illustrated in Fig. 8, the pressure difference and pressure derivative curves are shown for varying numbers of hydraulic fractures. As the number of fractures increases, the time required for the bottomhole pressure to reach the constraint pressure becomes longer. As demonstrated in Fig. 8, the CO_2 storage capacity curves illustrate that an increased number of fractures becomes progressively advantageous in enhancing CO_2 storage capacity at higher constraint pressures. This is because a larger number of fractures provides more pathways for CO_2 to enter the formation. Under the same injection rate, a smaller pressure difference is required, causing the bottomhole pressure to rise more slowly and reach the constrained pressure later.

In the context of a constraint pressure of 12 MPa, the calculated CO_2 storage capacities for 11, 15, and 21 fractures are 0.615 × 10^8 m,^{3} 1.025 × 10^8 m,^{3} and 1.810 × 10^8 m,^{3} respectively. The storage capacity with 21 fractures is 194.3% greater than that with 11 fractures. These results suggest that, at a constant injection rate, increasing the number of fractures can significantly enhance CO_2 storage capacity.

4.2.4. *Fracture spacing*

The pressure difference and pressure derivative curves for different fracture spacings are shown in Fig. 9. As the fracture spacing increases, the pressure response and its derivative shift later in time, indicating that interference between fractures occurs later in time. Furthermore, the time required for the bottomhole pressure to reach the constraint pressure also increases with larger fracture spacing. The CO_2 storage capacity curves shown in Fig. 9 indicate that both higher constraint pressure and larger fracture spacing lead to greater CO_2 storage capacity. At a constraint pressure of 12 MPa, the calculated CO_2 storage capacities for fracture spacings of 60 m, 100 m, and 140m are 0.615 × 10^8 m,^{3} 1.248 × 10^8 m,^{3} and 1.966 × 10^8 m,^{3} respectively. The storage capacity at a spacing of 140 m is 219.7% higher than that at 60 m. These results suggest that, at a constant injection rate, increasing fracture spacing can also significantly enhance CO_2 storage capacity.

4.2.5. *Hydraulic fracture conductivity*

As illustrated in Fig. 10, the pressure difference and pressure derivative curves are presented for various fracture conductivities. As fracture conductivity increases, the bilinear and linear flow regimes occur earlier, and the time required for the bottomhole pressure to reach the constraint pressure becomes slightly longer. Nevertheless, the disparities are comparatively negligible. At a constraint pressure of 12 MPa, the calculated CO_2 storage capacities for fracture conductivities of 50 mD·m, 100 mD·m, and 300 mD·m are 0.566 × 10^8 m,^{3} 0.615 × 10^8 m,^{3} and 0.652 × 10^8 m,^{3} respectively. The storage capacity for a conductivity of 300 mD·m is 15.2% higher than that for a conductivity of 50 mD·m. These results indicate that a higher fracture conductivity slightly improves CO_2 storage capacity, but the overall influence is relatively limited.

4.2.6. *Adsorption density*

The pressure difference and pressure derivative curves for different CO_2 adsorption densities are shown in Fig. 11. As the adsorption density increases, the upward shift in the pressure and derivative curves occurs at a later point in time. The adsorption effect causes part of the injected CO_2 to be adsorbed onto the rock surface, which reduces the fluid flow between grid cells. As a result, the required pressure difference decreases, leading to a slower increase in bottomhole pressure and a later arrival at the constrained pressure. As demonstrated in Fig. 11, the CO_2

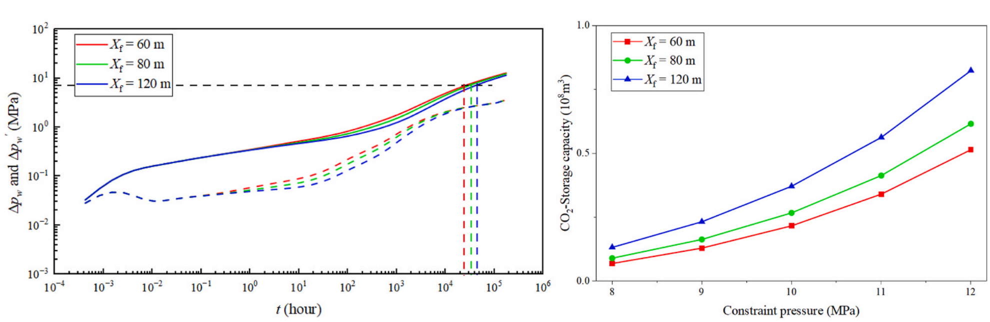

Fig. 7. Pressure curves and CO_2-storage capacity curves at different fracture half-lengths.

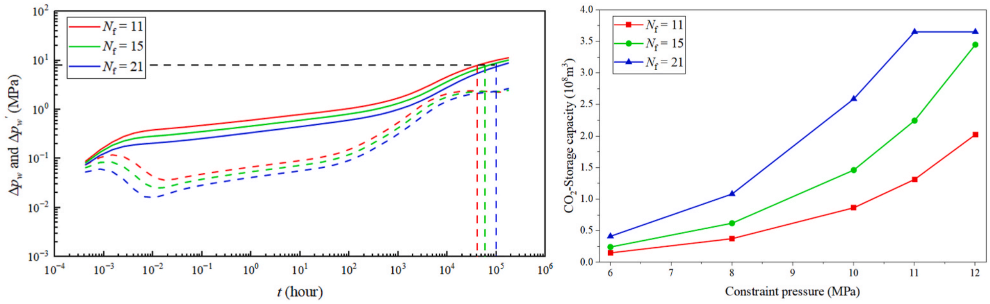

Fig. 8. Pressure curves and CO_2-storage capacity curves at different numbers of hydraulic fractures.

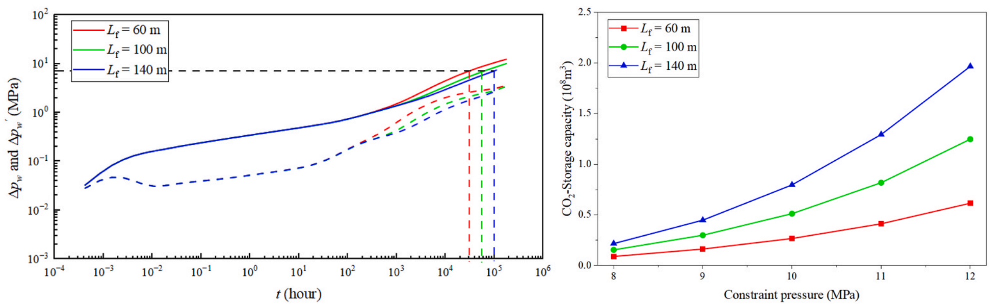

Fig. 9. Pressure curves and CO_2-storage capacity curves at different fracture spacings.

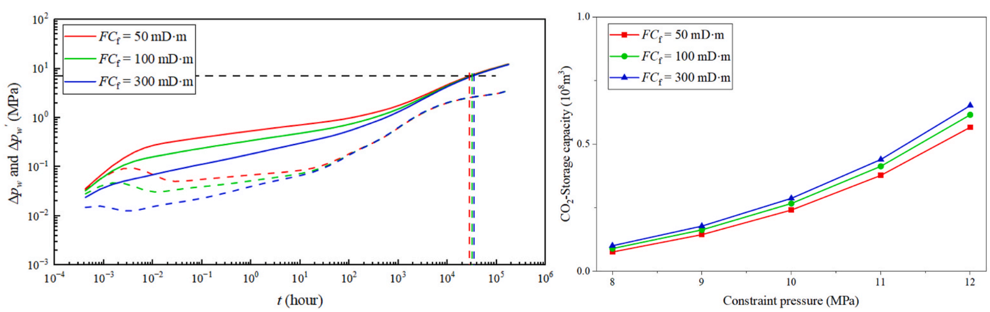

Fig. 10. Pressure curves and CO_2-storage capacity curves at different hydraulic fracture conductivities.

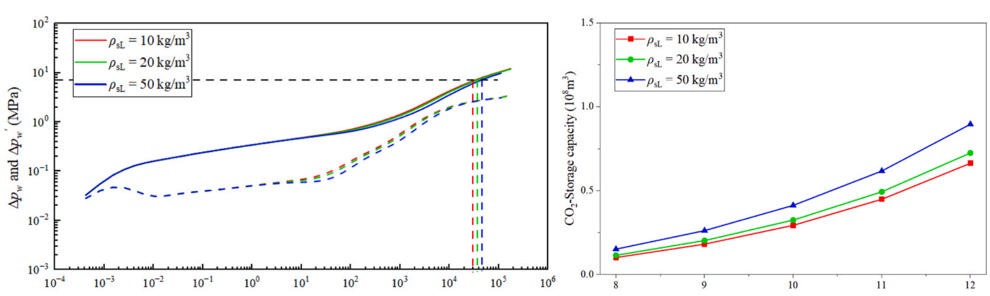

Fig. 11. Pressure curves and CO_2-storage capacity curves at different adsorption densities.

storage capacity curves indicate that an enhancement in CO_2 adsorption capacity can result in a substantial increase in CO_2 storage capacity. In the context of a constraint pressure of 12 MPa, the calculated CO_2 storage capacities for adsorption densities of 10 kg/m^3, 20 kg/m^3, and 50 kg/m^3 are 0.615×10^8 m,[3] 0.725×10^8 m,[3] and 0.896×10^8 m,[3] respectively. It is evident that the storage capacity at an adsorption density of 50 kg/m^3 is 45.7% higher than that at 10 kg/m^3. These results indicate that, at a constant injection rate, a higher CO_2 adsorption density can significantly enhance CO_2 storage capacity.

4.2.7. Diffusion coefficient

As illustrated in Fig. 12, the pressure difference and pressure derivative curves are shown for different diffusion coefficients. As the diffusion coefficient increases, the mid-time pressure and pressure derivative curves shift downward. The bottomhole pressure reaches the constraint pressure later, although the differences are relatively small. The CO_2 storage capacity curves at different diffusion coefficients are shown in Fig. 12. At a constraint pressure of 12 MPa, the calculated CO_2 storage capacities for diffusion coefficients of 0, 2.8×10^{-3} m^2/h, and $5.6 \times$

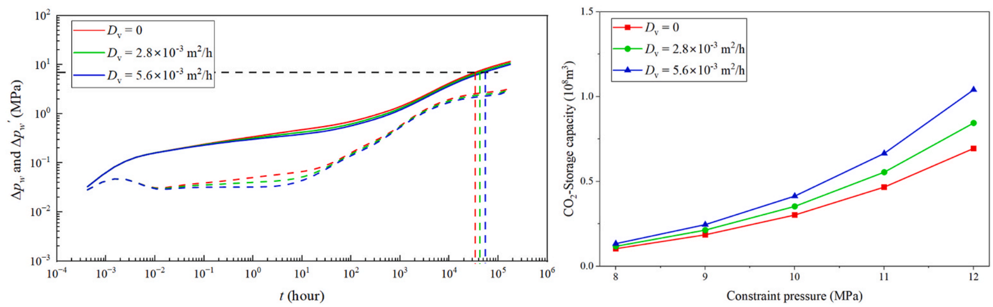

Fig. 12. Pressure curves and CO_2-storage capacity curves at different diffusion coefficients.

10^{-3} m^2/h are 0.615×10^8 m,^{3} 0.844×10^8 m,^{3} and 1.04×10^8 m,^{3} respectively. The storage capacity at a diffusion coefficient of 5.6×10^{-3} m^2/s is 69.1% higher than that at 0 m^2/h. These results suggest that a higher diffusion coefficient leads to greater CO_2 storage capacity.

4.2.8. Stress sensitivity coefficient

Fig. 13 presents the pressure difference and pressure derivative curves for different stress sensitivity coefficients. As the stress sensitivity coefficient increases, the rate of bottomhole pressure buildup in the late stage slows down, and the time required to reach the constraint pressure becomes longer. The CO_2 storage capacity curves at different stress sensitivity coefficients are shown in Fig. 13. At a constraint pressure of 12 MPa, the calculated CO_2 storage capacities for stress sensitivity coefficients of 0, 0.05 MPa^{-1}, and 0.20 MPa^{-1} are 0.846×10^8 m,^{3} 1.01×10^8 m,^{3} and 2.737×10^8 m,^{3} respectively. The CO_2 storage capacity at a coefficient of 0.20 MPa^{-1} is 223.5% higher than that at 0 MPa^{-1}. These results indicate that stress sensitivity can significantly enhance CO_2 storage capacity. As CO_2 is injected, the matrix pressure increases, and the matrix permeability correspondingly increases due to stress-sensitivity effects. As a result, the transmissibility between grid cells also increases. For a fixed injection rate, this leads to a reduction in the pressure difference between grid cells, thereby extending the time required for the bottomhole pressure to reach the constrained pressure.

5. Case study

Considering that there was a lack of pressure test data during the CO_2 injection process, parameter inversion was instead based on pressure test data from shale gas production. To demonstrate the workflow and practicality of the proposed CO_2 storage capacity evaluation method, a case study was conducted on a shale gas well (referred to as Well A) located in the Longmaxi Formation of the Sichuan Basin, China (see Fig. 14). Well A was completed in 2015 with a horizontal section approximately 1400 m long. In 2016, it underwent proppant hydraulic fracturing, comprising 21 stages. A total of 38,415 m^3 of fracturing fluid and 1483 m^3 of proppant were used. Microseismic monitoring and test reports indicated that the average half-length of the hydraulic fractures was approximately 80 m. Later, a pressure build-up test was performed in August 2016, following production at a daily gas rate of approximately 45,000 m^3/d. The produced gas composition was 97.48% methane and 0.49% ethane. The predominant orientation of natural fractures in this area is observed to be in the southeast–northwest and northwest–southeast directions. The ADFNE algorithm was employed to generate natural fractures corresponding to these orientations. For simplicity, it is assumed that the gas mixture consists only of methane and ethane, with methane accounting for 98% and ethane for 2%, while the injected gas is pure CO_2. The PVT parameters of the components are listed in Table 2.

As shown in Fig. 4, the following steps are to be taken to evaluate the CO_2 storage capacity of the shale reservoir. Firstly, a numerical well test model is constructed, and reservoir and fracture parameters are inferred from pressure-test data. Secondly, the numerical model is calibrated using inverted parameters. Thirdly, the injection rate and constrained pressure are determined based on the specifications of the injection equipment, the safety requirements, and other operational considerations. Finally, the calibrated numerical CO_2-injection well-test model is used to simulate the pressure transient behaviors during CO_2 injection and to compute the CO_2 storage capacity. The input parameters used in the model are listed in Table 3. The pressure difference and pressure derivative curves during the pressure build-up stage are shown in Fig. 15.

The model parameters (such as reservoir permeability, fracture conductivity, and wellbore storage coefficient) were iteratively adjusted, with the simulated results matched against the actual test data until a satisfactory curve match was achieved. The resulting model parameters are considered to be the history-matched reservoir properties. These history-matched model curves are displayed in Fig. 15(a), and the corresponding calibrated model parameters are listed in Table 4.

Due to the lack of pressure data during the CO_2 injection process, the history-matched reservoir parameters were obtained using pressure test data from shale gas production. It was assumed that the reservoir pressure had declined to 5 MPa after gas production, and that the in-situ gas composition consisted of 90% methane and 10% CO_2. A CO_2 injection numerical model was then established to simulate pressure transient behaviors at different injection rates over a 20-year period. The CO_2 storage capacity at various constraint pressures was also evaluated.

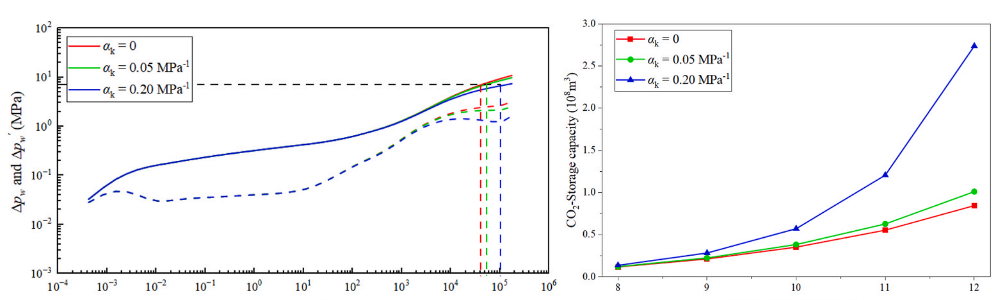

Fig. 13. Pressure curves and CO_2-storage capacity curves at different stress sensitivity coefficients.

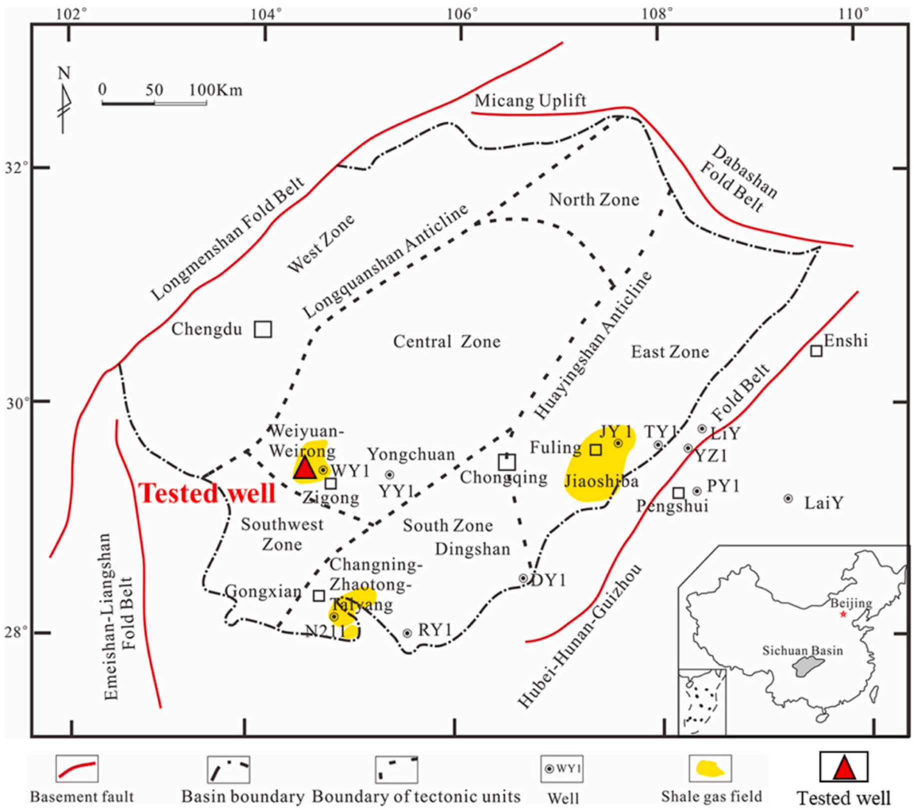

Fig. 14. Location map of the tested well in the Longmaxi formation (modified from Nie et al.[48]).

Table 2
Input parameters of the model.

Parameters	Carbon dioxide	Methane	Ethane	Unit
Critical Temperature	304.1	190.6	305.3	K
Critical Pressure	7.38	4.60	4.87	MPa
Critical molar volume	9.41×10^{-5}	9.86×10^{-5}	1.46×10^{-4}	m^3/mol
Molecular weight	44.01	16.04	34.07	g/mole

Table 3
Input parameters of the model.

Parameters	Value	Unit
Initial pressure	40	MPa
Formation size	2000 × 2000 × 20	m
Porosity	0.08	/
Hydraulic fracture half-length	80	m
Number of natural fractures	500	/
Average length of natural fractures	60	m
Natural fracture conductivity	5	mD·m

The results are shown in Fig. 15(b) and (c).

As shown in Fig. 15, the pressure and derivative curves shift upward with increasing injection rates, while consistently exhibiting the identified flow regimes. The curves transition from wellbore storage through linear flow into the inter-fracture interference stage. Subsequently, the derivative reflects the characteristics of elliptical flow before finally reaching the pseudo-radial flow stage. The upward shift across all these regimes indicates that higher rates accelerate the pressure rise, shortening the time to reach the constraint pressure and thus limiting the total CO_2 storage capacity. Furthermore, the CO_2 storage capacity is jointly influenced by both the injection rate and the constraint pressure. When the constraint pressure is 8 MPa, a higher injection rate causes the bottomhole pressure to reach the constraint pressure earlier, thereby reducing the overall CO_2 storage capacity. Conversely, at higher constraint pressures, lower injection rates may fail to reach the constraint pressure by the end of the simulation, thus underutilizing the reservoir's storage potential. Specifically, the maximum CO_2 storage capacity for Well A was achieved at an injection rate of 8000 m^3/d and a constraint pressure of 9 MPa, 10,000 m^3/d at 11 MPa, and 12,000 m^3/day at a constraint pressure of 12 MPa. These results indicate that both the injection rate and the constraint pressure must be optimized simultaneously to maximize the potential for CO_2 sequestration.

Furthermore, comparing the pressure distribution at different injection rates (see Fig. 16) reveals that higher injection rates accelerate pressure propagation and CO_2 migration into the reservoir. However, they also cause a rapid increase in pressure near the fractured horizontal well and the surrounding reservoir, resulting in the bottomhole pressure reaching the constraint pressure prematurely. This further highlights the importance of simultaneously optimizing both the injection rate and the constraint pressure to enhance CO_2 storage capacity.

6. Conclusions

In this study, an analytically projected embedded discrete fracture model was proposed for simulating transient fluid flow. The model was applied to analyze the pressure transient behaviors during CO_2 injection in shale gas reservoirs and to evaluate the corresponding CO_2 storage capacity. The main conclusions are as follows:

(1) The proposed AEDFM projects fractures onto all six faces of the matrix cells and establishes direct connections between the fractures and adjacent matrix cells, thereby accounting for the influence of the surrounding matrix on early-time transient flow. The results demonstrate that AEDFM can accurately simulate the pressure transient behaviors during CO_2 injection.

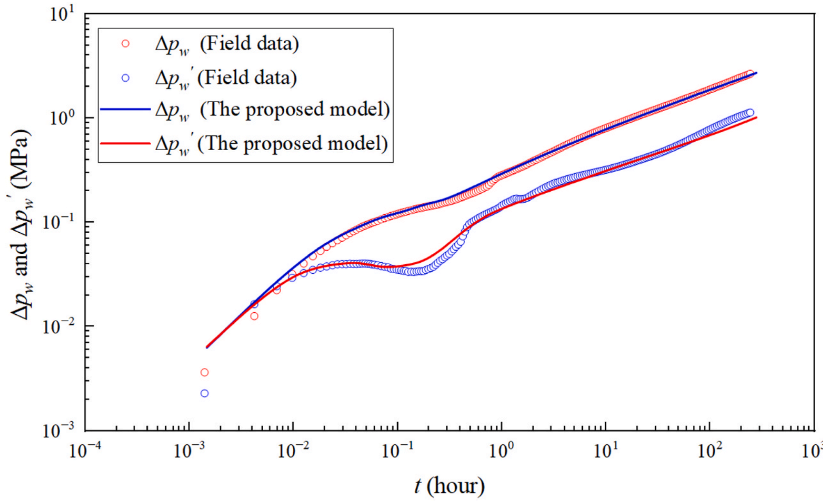

(a) The results of curve matching.

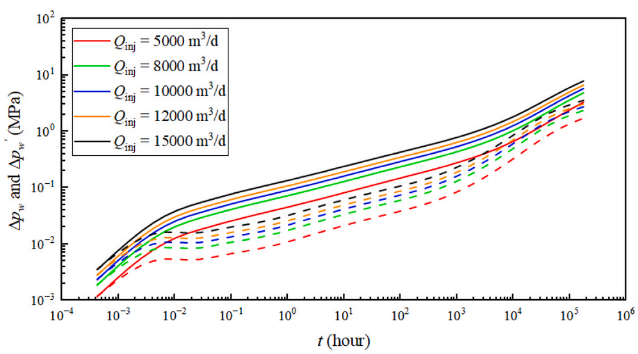

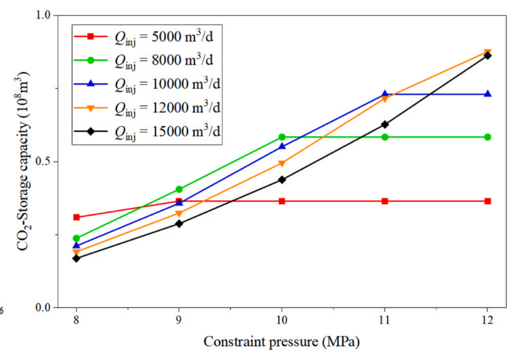

(b) Pressure curves. (c) CO_2 storage capacity curves.

Fig. 15. The curve matching results, pressure curves and CO_2 storage capacity curves of Well A.

Table 4
History-matched reservoir parameters.

Parameters	Value	Unit
Permeability	5×10^{-3}	mD
Hydraulic fracture conductivity	50	mD·m
Wellbore storage coefficient	1.6	m^3/MPa
Skin factor	2×10^{-4}	/

(2) The flow regimes of the MFHW during CO_2 injection can be divided into six stages: wellbore storage and skin effects, bilinear flow, linear flow, inter-fracture interference, elliptical flow, and pseudo-radial flow.

(3) The CO_2 storage capacity of the reservoir is influenced by multiple factors, including injection duration, injection rate, constraint pressure, and permeability. It is important to note that an elevated injection rate does not invariably lead to an increase in CO_2 storage capacity. For instance, in this study, at a constraint pressure of 10 MPa, the injection rate of 40,000 m^3/d yielded the highest storage capacity, followed by 10,000 m^3/d, while the lowest storage capacity was observed at an injection rate of 100,000 m^3/d.

(4) Under constant injection rate conditions, increasing the fracture half-length, number of fractures, and fracture spacing can effectively enhance CO_2 storage capacity, although the influence of fracture conductivity is relatively limited. Additionally, higher CO_2 adsorption density and diffusion coefficient contribute significantly to increasing CO_2 storage capacity.

(5) Reservoir parameters such as permeability were obtained through history matching based on pressure test data from a shale gas well in the Longmaxi Formation. The CO_2 storage capacity at different injection rates was then evaluated using the history-matched parameters, demonstrating the practicality of the proposed method for assessing CO_2 storage capacity.

Despite its accuracy in characterizing pressure transient behaviors, this study has certain limitations. The current framework adopts isothermal and closed boundary assumptions to isolate the influence of key parameters on CO_2 storage capacity. While this is reasonable for interpreting bottom-hole pressure where thermal and boundary effects are secondary during the transient period, it may not fully capture long-term coupled thermal-hydro effects or complex geological connectivity.

Future research will focus on extending the AEDFM to include energy balance equations, diverse boundary conditions, and optimized injection strategies to provide a more comprehensive and practical assessment of long-term storage security in complex fractured reservoirs.

CRediT authorship contribution statement

Zhiming Chen: Writing – review & editing, Validation, Software, Methodology, Conceptualization. **Biao Zhou:** Writing – original draft, Visualization, Validation, Software, Methodology, Investigation. **Olufemi Olorode:** Writing – review & editing, Software, Methodology. **Wei**

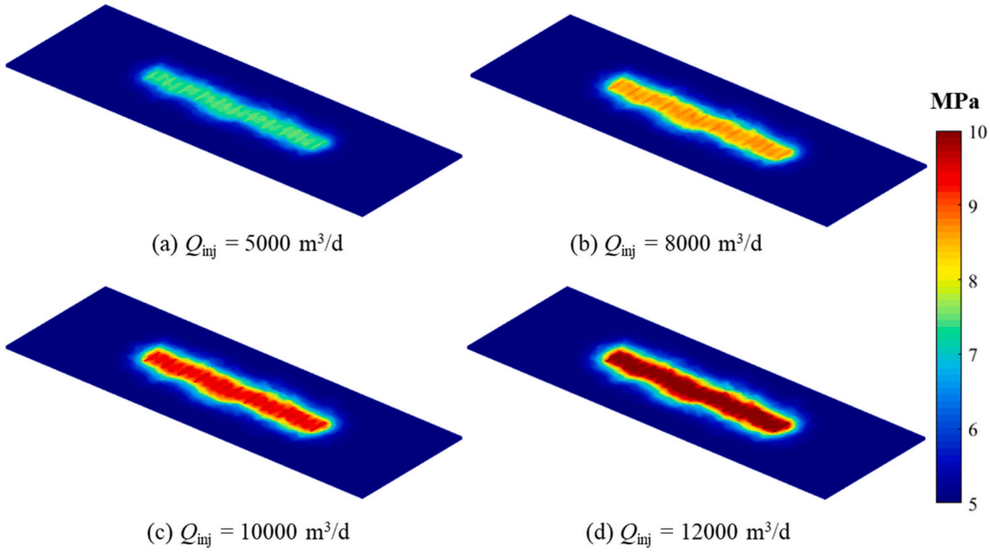

Fig. 16. Pressure distribution at different injection rates at the 12th year of injection.

Yu: Writing – review & editing, Software, Methodology. **Kamy Sephrnoori:** Writing – review & editing, Supervision, Methodology.

Declaration of competing interest

The authors declare that they have no known competing financial interests or personal relationships that could have appeared to influence the work reported in this paper.

Acknowledgement

The authors would like to thank all those who contributed to improving this work. The authors also acknowledge financial support from the Hainan Provincial Natural Science Foundation of China (426YXQN0960), the Beijing Nova Program (20230484249), the National Natural Science Foundation of China (52274046), and Oil & Gas Major Projects (2025ZD1401400, 2025ZD1404106 & 2025ZD1408302). This paper is an improvement for a conference presentation (SPE 225302), and the full copyright of the presentation has been reverted to the original owner.

Data availability

Data will be made available on request.

References

1. Middleton RS, Carey JW, Currier RP, et al. Shale gas and non-aqueous fracturing fluids: opportunities and challenges for supercritical CO2. *Appl Energy*. 2015;147: 500–509.
2. Li X, Elsworth D. Geomechanics of CO2 enhanced shale gas recovery. *J Nat Gas Sci Eng*. 2015;26:1607–1619.
3. Zhang K, Jin Z, Li S. Coupled miscible carbon utilization-storage processes in fractured shales. *Chem Eng J*. 2022;441, 135987.
4. Mohagheghian E, Hassanzadeh H, Chen Z. CO2 sequestration coupled with enhanced gas recovery in shale gas reservoirs. *J CO2 Util*. 2019;34:646–655.
5. Tayari F, Blumsack S. A real options approach to production and injection timing under uncertainty for CO2 sequestration in depleted shale gas reservoirs. *Appl Energy*. 2020;263, 114491.
6. Lee Y, Song I, Park C. Analytical assessment of CO2-storage efficiency and geomechanical-coupling behaviors using poromechanical experiments. *Int J Rock Mech Min Sci*. 2025;196, 106320.
7. Li X, Zhang F, Guo T, Zhou C. Effects of CO2-water-rock interactions on the fracture performance of transversely isotropic shale: transition from strengthening to weakening. *Int J Rock Mech Min Sci*. 2026;199, 106435.
8. Shchipanov A, Kollbotn L, Berenblyum R. Characterization and monitoring of reservoir flow barriers from pressure transient analysis for CO2 injection in saline aquifers. *Int J Greenh Gas Control*. 2019;91, 102842.
9. Chu H, Liao X, Chen Z, Liu W, Mu L, Liu H. A new methodology to assess the maximum CO2 geosequestration capacity of shale reservoirs with SRV based on wellbore pressure. *J CO2 Util*. 2019;34:239–255.
10. Su K, Liao X, Zhao X. Transient pressure analysis and interpretation for analytical composite model of CO2 flooding. *J Petrol Sci Eng*. 2015;125:128–135.
11. Chen Z, Liao X, Zhao X, Feng X, Zang J, He L. A new analytical method based on pressure transient analysis to estimate carbon storage capacity of depleted shales: a case study. *Int J Greenh Gas Control*. 2015;42:46–58.
12. Xiao C, Tian L, Yang Y, Zhang Y, Gu D, Chen S. Comprehensive application of semi-analytical PTA and RTA to quantitatively determine abandonment pressure for CO2 storage in depleted shale gas reservoirs. *J Petrol Sci Eng*. 2016;146:813–831.
13. Fiallos MX, Yu W, Ganjdanesh R, et al. *Modeling Interwell Interference due to Complex Fracture Hits in Eagle Ford Using EDFM. International petroleum technology conference*. IPTC; 2019, D011S009R001.
14. Hui M-H, Mallison B, Thomas S, et al. *A hybrid embedded discrete fracture model and dual-porosity. Dual-Permeability Workflow for Hierarchical Treatment of Fractures in Practical Field Studies*. SPE Reservoir Evaluation & Engineering; 2023:1–17.
15. Rao X, Cheng L, Cao R, et al. An efficient three-dimensional embedded discrete fracture model for production simulation of multi-stage fractured horizontal well. *Eng Anal Bound Elem*. 2019;106:473–492.
16. Xiang Z, Zhen R, Xu Y, et al. A numerical pressure transient model of fractured well with complex fractures of tight gas reservoirs considering gas-water two phase by EDFM. *Geoenergy Sci Eng*. 2023;231, 212286.
17. Zhang H, Sheng JJ. An efficient embedded discrete fracture model based on the unstructured quadrangular grid. *J Nat Gas Sci Eng*. 2021;85, 103710.
18. Yang J, Xue F, Liu J, Chen B, Dai J. A hybrid multiscale model for fluid flow in fractured rocks using homogenization method with discrete fracture networks. *Int J Rock Mech Min Sci*. 2024;183, 105936.
19. Yu W, Xu Y, Liu M, Wu K, Sepehrnoori K. Simulation of shale gas transport and production with complex fractures using embedded discrete fracture model. *AIChE J*. 2018;64(6):2251–2264.
20. Ţene M, Bosma SBM, Al Kobaisi MS, Hajibeygi H. Projection-based embedded discrete fracture model (pEDFM). *Adv Water Resour*. 2017;105:205–216.
21. Yu W, Xu Y, Weijermars R, Wu K, Sepehrnoori K. A numerical model for simulating pressure response of well interference and well performance in tight oil reservoirs with complex–fracture geometries using the fast embedded–discrete–fracture–model method. *SPE Reservoir Eval Eng*. 2017;21(2):489–502.
22. Liu H, Liao X, Zhao X, Sun L, Tang X, Zhao L. A high-resolution numerical well-test model for pressure transient analysis of multistage fractured horizontal wells in naturally fractured reservoirs. *J Petrol Sci Eng*. 2022;208, 109417.
23. Rao X. A generic workflow of projection-based embedded discrete fracture model for flow simulation in porous media. *Comput Geosci*. 2023;27(4):561–590.
24. Xu Y, Sepehrnoori K. Modeling fracture transient flow using the embedded discrete fracture model with nested local grid refinement. *J Petrol Sci Eng*. 2022;218, 110882.
25. Losapio D, Scotti A. Local Embedded Discrete Fracture Model (LEDFM). *Adv Water Resour*. 2023;171, 104361.
26. Olorode O, Rashid H. Analytical modification of EDFM for transient flow in tight rocks. *Sci Rep*. 2022;12(1), 22018.
27. Zhou B, Chen Z, Song Z, Tang Z, Wang B, Olorode O. A new analytically modified embedded discrete fracture model for pressure transient analysis in fluid flow. *J Hydrol*. 2024;636, 131330.
28. Jiao K, Yu M, Li Y, et al. Handling fracture intersections in the enriched-embedded discrete fracture model (nEDFM). *Adv Water Resour*. 2026;207:105198.
29. Jiang J, Younis RM. An improved projection-based embedded discrete fracture model (pEDFM) for multiphase flow in fractured reservoirs. *Adv Water Resour*. 2017; 109:267–289.

30. Rao X, Cheng L, Cao R, Jia P, Liu H, Du X. A modified projection-based embedded discrete fracture model (pEDFM) for practical and accurate numerical simulation of fractured reservoir. *J Petrol Sci Eng*. 2020;187, 106852.
31. Olorode O, Wang B, Rashid HU. Three-dimensional projection-based embedded discrete-fracture model for compositional simulation of fractured reservoirs. *SPE J*. 2020;25(4):2143–2161.
32. Rashid HU, Olorode O. A continuous projection-based EDFM model for flow in fractured reservoirs. *SPE J*. 2023:1–17.
33. Liu L, Wang X, Lei Q. Effects of secondary fractures on fault seismic rupture and aseismic slip during CO2 sequestration. *Int J Rock Mech Min Sci*. 2026;200, 106456.
34. Chen Z, Zhao X, Zhu H, et al. Engineering factor analysis and intelligent prediction of CO2 storage parameters in shale gas reservoirs based on deep learning. *Appl Energy*. 2025;377, 124642.
35. Zuloaga-Molero P, Yu W, Xu Y, Sepehrnoori K, Li B. Simulation study of CO2-EOR in tight oil reservoirs with complex fracture geometries. *Sci Rep*. 2016;6(1), 33445.
36. Zhao X, Chen Z, Wang B, Liao X, Li D, Zhou B. A Multi-medium and Multi-mechanism model for CO2 injection and storage in fractured shale gas reservoirs. *Fuel*. 2023;345, 128167.
37. Jia Z, Cheng L, Feng H, et al. Full composition numerical simulation of CO2 utilization process in shale reservoir using projection-based embedded discrete fracture model (pEDFM) considering nano-confinement effect. *Gas Sci Eng*. 2023; 111, 204932.
38. Zhang K, Jin Z, Li G, Liu Q, Tian L. Gas adsorptions of geological carbon storage with enhanced gas recovery. *Separ Purif Technol*. 2023;311, 123260.
39. Hou B, Li Z, Yang W, Gao Y, Wang Y, Hao Z. Impact of hydraulic fracturing combined with CO2 gas injection displacement on coalbed methane extraction. *Int J Rock Mech Min Sci*. 2026;202, 106491.
40. Chen Z, Zhou B, Yu W, Sepehrnoori K. A numerical well test model for fractured Wells in fractured shale gas reservoirs considering multiple flow mechanisms. *SPE J*. 2025:1–16.
41. Zhang Y, Jin Y, Yang D. Semi-analytical modeling of transient pressure behaviour for a multifractured horizontal well in a gas reservoir with a complex fracture network by considering effects of slippage, stress-sensitivity, and gas adsorption/desorption. *J Petrol Sci Eng*. 2022;214, 110504.
42. Lie K-A. *An Introduction to Reservoir Simulation Using MATLAB/GNU Octave: User Guide for the MATLAB Reservoir Simulation Toolbox (MRST)*. Cambridge University Press; 2019.
43. Lie K-A, Møyner O. *Advanced Modelling with the MATLAB Reservoir Simulation Toolbox*. Cambridge University Press; 2021.
44. Myshakin EM, Singh H, Sanguinito S, Bromhal G, Goodman AL. Flow regimes and storage efficiency of CO2 injected into depleted shale reservoirs. *Fuel*. 2019;246: 169–177.
45. Zeng H, Fan D, Yao J, Sun H. Pressure and rate transient analysis of composite shale gas reservoirs considering multiple mechanisms. *J Nat Gas Sci Eng*. 2015;27: 914–925.
46. Zhao X, Chen Z, Zhang L, Liao X, Awotunde AA. Leakage risk assessment on sealing efficiency of caprock during CO2 huff-n-puff for safe sequestration. *Geoenergy Sci Eng*. 2024;240, 213056.
47. Alghalandis YF. ADFNE: open source software for discrete fracture network engineering, two and three dimensional applications. *Comput Geosci*. 2017;102: 1–11.
48. Nie H, Chen Q, Zhang G, Sun C, Wang P, Lu Z. An overview of the characteristic of typical Wufeng–Longmaxi shale gas fields in the Sichuan Basin, China. *Nat Gas Ind B*. 2021;8(3):217–230.